

# COMPTONIZATION OF THERMAL PHOTONS BY RELATIVISTIC ELECTRON BEAMS

JOSEPH K. DAUGHERTY<sup>1</sup>

Department of Computer Science, University of North Carolina at Asheville

AND

ALICE K. HARDING

Laboratory for High Energy Astrophysics, NASA/Goddard Space Flight Center

Received 1988 April 25; accepted 1988 June 23

## ABSTRACT

We have developed a numerical calculation of gamma-ray emission produced by Compton scattering of relativistic electron beams on background thermal radiation, which includes spatial dependence of electron energy losses and cyclotron resonance scattering in a strong magnetic field. Monte Carlo simulation is used to follow a sample of electrons from an injection zone, tracing each electron through multiple scattering events. Both the development of the inverse Compton gamma-ray spectrum and the electron energy losses are traced as the beam propagates through the ambient radiation field. In the first version, the scattering is described by the fully relativistic Klein-Nishina cross section, but the magnetic field is neglected. In the second version, the scattering is described by the magnetic resonant cross section in the Thomson limit. We find that when the magnetic field is not included, electron energy losses are important only at higher neutron star surface temperatures ( $T \sim 3 \times 10^6$  K). In the presence of a strong magnetic field ( $10^{12}$  G), resonant scattering greatly increases electron energy losses, making scattering very efficient even at lower surface temperatures. Resulting photon and electron spectra for both cases are discussed in relation to models for pulsar X-ray and gamma-ray emission.

*Subject headings:* gamma rays: general — pulsars — radiation mechanisms

## I. INTRODUCTION

Models of pulsar magnetospheres generally involve very high energy electron beams, produced by electrostatic acceleration near the stellar surface (Sturrock 1971; Ruderman and Sutherland 1975; Arons 1983), in the vicinity of the light cylinder (Gold 1968), or in intermediate zones such as the “outer gaps” (Cheng and Ruderman 1977; Cheng, Ho, and Ruderman 1986). In most of these models, Comptonization of the electron beams on ambient photons (thermal radiation from the stellar surface, curvature radiation, or perhaps synchrotron emission) may produce hard X-ray or gamma-ray emission in the MeV range. The large number of secondary electron-positron pairs produced in cascades near the polar cap (of order  $10^4$  per primary electron) possess energies of  $10^2$ – $10^4$  MeV, even after strong initial losses due to synchrotron radiation (Daugherty and Harding 1982). These secondary pairs should undergo Comptonization with the intense thermal radiation field at the stellar surface. The steady point source observed by the *Einstein* high-resolution imager at the position of the Vela pulsar implies a surface temperature of  $\sim 10^6$  K if this emission is in fact thermal (Harnden *et al.* 1985). The *Einstein* upper limit for the surface temperature of the Crab pulsar is  $3 \times 10^6$  K (Helfand *et al.* 1980; Harnden and Seward 1984). If pulsar surface temperatures are near  $10^6$  K, scattered gamma rays may reach energies of 10 MeV or even higher, and should add a significant contribution to the overall gamma-ray spectrum in the MeV range.

Previous analytical studies of inverse Compton scattering have produced well-known results in the case of isotropic electron and photon distributions (see, for example, Blumenthal and Gould 1970) and for electron beams (Reynolds 1982) in the

nonrelativistic (Thomson) limit. Jones (1968) has also considered the case of a relativistic electron beam traversing a monoenergetic, isotropic radiation field using the Klein-Nishina cross section.

Unfortunately, the analytical results do not extend to the case of a relativistic electron beam traversing a thermal (or other) energy distribution of photons, when the scattering cross section is not confined to the Thomson limit and the electron energy losses are significant. Even more serious for the pulsar surface acceleration models is the fact that the intense magnetic field ( $B \sim 10^{12}$  G) greatly affects the Compton scattering process, resulting in resonances in the scattering cross section (Canuto, Lodenguai, and Ruderman 1971; Herold 1979; Daugherty and Harding 1986). Thermal soft X-ray photons will be in or near the cyclotron resonance ( $\sim 10$  keV in fields of  $10^{12}$  G) in the rest frame of a relativistic electron and will therefore undergo resonant scattering with a cross section about  $10^3$  times Thomson. Two important consequences of this resonant behavior are an increase in the optical depth of the scattering regions, and greatly increased electron energy-loss rates (Xia *et al.* 1985), strongly affecting the spectra, angular distribution, and polarization properties of the Comptonized photons. Due to the complexity of these resonance effects, it appears necessary to use numerical techniques to derive quantitative estimates of Comptonization effects in pulsar magnetospheres.

Compton scattering in pulsar magnetospheres has previously been studied in a number of cases. Cheng and Ruderman (1977) and Elitzur (1979) considered the scattering of radio photons by electron-positron pairs to produce the optical radiation of the Crab pulsar. Tadamaru and Greenstein (1974) considered Compton scattering as a source of energy loss for relativistic electrons near the neutron star surface.

<sup>1</sup> Also University of Maryland.

Morini (1983), Schlickeiser (1980) and Cheng, Ho, and Ruderman (1986) proposed that the high-energy pulsed emission from the Crab and Vela could be due to Compton scattering by relativistic electrons. However, those studies which treated Comptonization near the neutron star surface did not include the effects of resonant scattering in a strong magnetic field. Ochelkov and Usov (1983) did include the effect of the pulsar magnetic field, but in the limit where scattering occurs well below the cyclotron resonance. Blandford and Scharlemann (1976) and Xia *et al.* (1985) calculated the energy loss of relativistic electrons due to resonant scattering of thermal photons from the neutron star surface, but they did not calculate the spectrum of the scattered photons or allow for a spatially dependent cyclotron resonance frequency and electron energy loss.

In this paper, we present numerical calculations of gamma-ray emission produced by Compton scattering of relativistic electron beams in thermal radiation fields. Monte Carlo simulation is used to follow a sample of electrons with either monoenergetic or power-law spectra from an injection point through multiple scattering events, allowing for spatial dependence of the electron spectrum and angular distribution (spreading of the beam). In § II a general description of two versions of the calculation is given. In the first version, the scattering is described by the fully relativistic Klein-Nishina cross section, but the intense pulsar magnetic fields are neglected. The second version takes into account the resonant behavior of the Compton cross section in superstrong magnetic fields, but only in the nonrelativistic (Thomson) limit. In § III we discuss the resulting spectra for the nonmagnetic and magnetic cases. Finally, we discuss the relevance of these results to models of pulsar X-ray and gamma-ray emission.

## II. DESCRIPTION OF CALCULATION

### a) Simulation of Beam Comptonization

We have developed two versions of electron beam scattering simulations. Version 1 is the “field-free” case, which employs standard Compton cross sections and kinematics, and hence ignores any effects of an ambient magnetic field on the scattering process. This version is not appropriate for pulsar surface acceleration models, except perhaps in the case of the millisecond pulsars which have extremely low surface fields ( $\sim 10^8$  G). We have included the field-free case here primarily to identify the effects of the magnetic field on the scattering. Version 2 includes resonant Compton cross sections, valid in the low-energy Thomson limit, to simulate scattering in a strong, spatially varying magnetic field. This version is more appropriate for applications in which electrons are accelerated near the stellar surface. Both versions are similar in their basic approach, and we will discuss their common features first.

Each version uses Monte Carlo simulation to trace multiple Compton scatterings of relativistic electrons as they traverse an ambient radiation field. The electrons are assumed to be purely beamed at their source, which is taken to be a localized region (e.g., a polar cap near the stellar surface) beyond which no further acceleration occurs. The beam axis is chosen as the  $z$ -direction, which is also the magnetic field direction in version 2. For the calculations described in § III below, we have considered electrons injected with either monoenergetic or power-law energy distributions, although more general spectral forms can easily be accommodated.

The simulation traces a large sample of electrons from their injection point, following the energy losses suffered by each

electron as it undergoes multiple scatterings on thermal background photons. The tracking continues as the electron propagates outward through the magnetosphere, until its energy has been degraded below a specified cutoff value, or until it has effectively escaped the ambient radiation field. The  $z$ -coordinate of each scattering event is recorded, so that the spatial evolution of both the electron and the Comptonized gamma-ray spectrum can be traced.

Each Compton scattering event is simulated by first evaluating the local mean free path  $\lambda = c/R$  for the electron in the radiation field, where the scattering rate  $R$  is given by the expression

$$R(E) = \int \omega^2 d\omega \int d\mu f_\gamma(\omega, \mu) \sigma_c(E, \omega, \mu)(1 - v\mu). \quad (1)$$

Here  $E$  and  $v$  denote the energy and velocity of the incident electron, while  $\omega$  and  $\mu$  are the energy and the cosine of the polar angle for the incoming photon. (We use natural units,  $\hbar = c = 1$ , throughout.) The factor  $f_\gamma(\omega, \mu)$  is the distribution function for the thermal photons. For the calculations described below, the thermal photon field has been taken as uniform and semi-isotropic, which is appropriate just above the stellar surface (where essentially all the high-energy Comptonization is found to occur). Thus we have assumed  $f_\gamma(\omega, \mu)$  to be of the form

$$f_\gamma(\omega, \mu) = \frac{1}{4\pi^3} \frac{1}{e^{\omega/kT} - 1}, \quad 0 \leq \mu \leq 1. \quad (2)$$

For stellar temperatures much lower than those considered here ( $T_6 \equiv T/10^6 \text{ K} \gtrsim 1$ ) the decrease in photon density with height above the stellar surface must be taken into account.

The quantity  $\sigma_c$  in equation (1) denotes the (invariant) total Compton cross section. One of the essential differences between versions 1 and 2 of the calculation is the choice of the cross section to be inserted here. The cross sections and mean free paths used in each version will be described fully in §§ IIb and IIc below. In either case, if the local mean free path is found to be smaller than the other limiting scales (i.e., the length scales for variations in the thermal photon densities and/or the ambient magnetic field), then the distance to the next scattering event is sampled exponentially. Otherwise the electron advances in steps smaller than the shortest length scale involved, and the mean free path is reevaluated at each step. The probability of scattering at each step is estimated and compared with a random number to “decide” whether a scattering event occurs at that step.

For each scattering event, the energy and polar angle of the incident photon are sampled using the integrand of the rate expression (eq. [1]). This part of the calculation requires different sampling methods for the two versions, which will be described in §§ IIb and IIc below. Once the location of the scattering event and the parameters of the incident photon have been selected, sampling of the polar angle and energy of the scattered photon must be carried out. This is done by first transforming to the Lorentz frame in which the electron is initially at rest (RF). The differential cross section is used to sample the scattered photon polar angle, which in the RF is measured with respect to the incident photon direction. After a value for the scattering angle has been sampled, the scattered photon energy is then determined by the kinematics. Both parameters are then used to transform back into the “laboratory” frame (LF).

The scattered photons, as seen in the LF, are strongly beamed, with most polar angles very nearly parallel to the direction of the electron beam. These small beaming angles greatly reduce the likelihood [by roughly the factor  $(1 - v\mu)$ ] that the scattered photons will suffer further Compton collisions. Hence each version of the present calculation assumes that each photon (unlike the electrons) scatters only once. Thus the scattered photon is immediately added to the appropriate bin in a three-dimensional table of "final" photon counts, where the table dimensions correspond to the  $z$ -coordinate (height), the energy, and the polar angle of the scattered photon.

The evolution of the electrons is also traced by binning them into similar tables. After each new scattering event, the appropriate table entries between the starting and stopping  $z$ -values are incremented. In the field-free case (version 1), these tables are three-dimensional (ranging over electron polar angle as well as height and energy). In version 2 the electrons are assumed to remain parallel to the magnetic field direction after each scattering event, and hence require tables only over height and energy. This assumption is equivalent to the approximation that all magnetic scattering events leave the electrons in their lowest Landau orbitals; for a discussion of more general Compton scattering events see Daugherty and Harding (1986). It might be noted that the electron beam angular dispersions in field-free scattering are quite small (typically  $\Delta\mu \leq 10^{-4}$  for all the calculations discussed in § III below). Hence the single-scattering approximation used for the photons remains valid as the electron beam propagates upward.

At the end of the simulation, the accumulated tables are used to derive and plot such quantities as the energy spectra for both the photons and electrons, and the angular distributions of the emergent Comptonized photons.

#### b) Field-free Compton Scattering

For version 1 of our calculation (field-free scattering), we have used the relativistic Klein-Nishina total cross section in equation (1), which may be written in the form (Berestetskii, Lifshitz, and Pitaevskii 1982)

$$\sigma_c = \frac{3\sigma_T}{4} \frac{1}{x} \left[ \left( 1 - \frac{4}{x} - \frac{8}{x^2} \right) \ln(1+x) + \frac{1}{2} + \frac{8}{x} - \frac{1}{2(1+x)^2} \right]. \quad (3)$$

Here  $x$  denotes the Lorentz-invariant quantity  $2p_\mu k^\mu/m^2$ , where  $p^\mu$  and  $k^\mu$  are the incident electron and photon momentum 4-vectors. In the RF, the scalar  $x$  is equal to  $2\omega_R/m$ , and for small  $x$  (the Thomson limit) the cross section becomes approximately

$$\sigma_c \sim \sigma_T(1-x). \quad (4)$$

Here the leading term is just the Thomson cross section,  $\sigma_T$ . Since we have used the exact form (3), the mean free paths determined from evaluation of equation (1) are valid even when the incident (RF) photon energies extend well above the Thomson limit.

The incident photon energy and polar angle are sampled from the differential scattering rate (cf. Fig. 1), which is the integrand of equation (1) with the cross section given in equation (3). Since the distributions of incident photon energy and polar angle as derived from the differential cross section are correlated in the Klein-Nishina limit, we use a Von Neumann rejection technique to sample the energy and polar angle of the incident photon simultaneously.

For the sampling of the scattered photon angle  $\eta = \cos \Theta$  measured with respect to the incident photon direction in the RF, we have used the relativistic (Klein-Nishina) differential

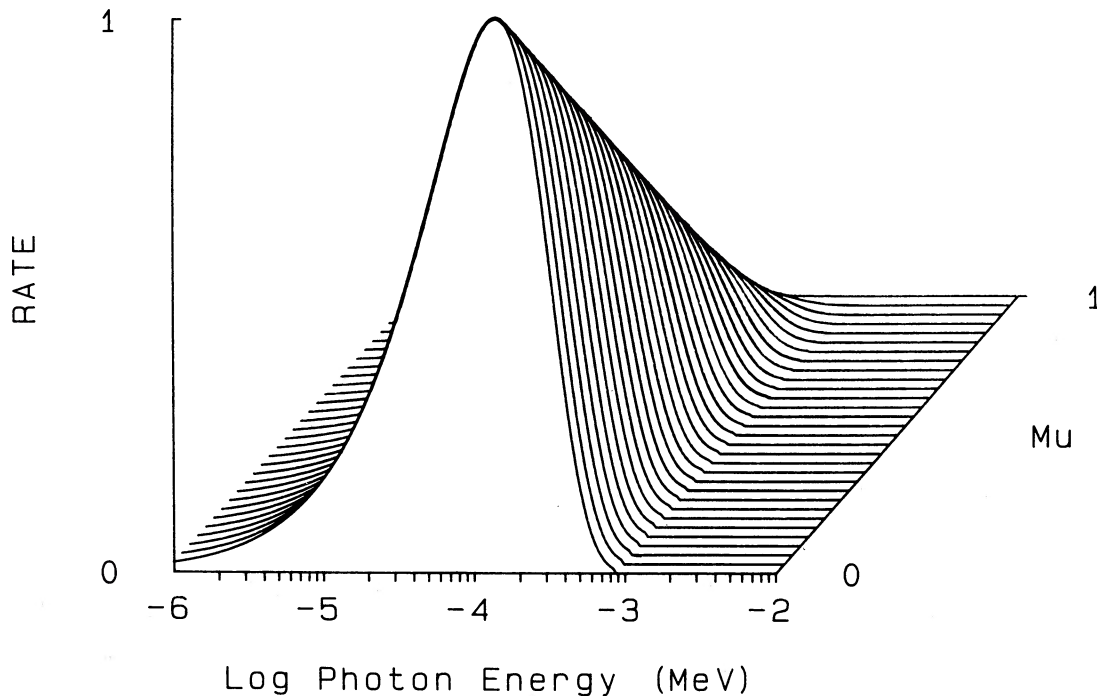


FIG. 1.—Nonmagnetic differential scattering rate function  $R(\omega, \mu)$  (eq. [1]) for  $T_e = 1$ . Distribution is normalized so that the peak value is unity.

cross section, which may be expressed in the form (Heitler 1954)

$$d\sigma_C = \frac{3\sigma_T}{8\pi} d\Omega' \frac{(1+\eta)^2}{2[1+(x/2)(1-\eta)]^2} \times \left\{ 1 + \frac{x^2(1-\eta)^2}{4(1+\eta^2)[1+(x/2)(1-\eta)]^2} \right\}, \quad (5)$$

where  $d\Omega' = d\eta d\phi$ . Once the scattering angle is sampled from this distribution, the corresponding scattered RF photon energy  $\omega'_R$  is obtained from the well-known kinematical relation

$$\omega'_R = \frac{\omega_R}{1 + (\omega_R/m)(1-\eta)}. \quad (6)$$

### c) Magnetic Compton Scattering

There are several complications which arise from the magnetic scattering cross section used in version 2 of the calculation. In order to simplify our initial treatment as much as possible, we have used the Thomson limit of the total cross section (Canuto, Lodenquai, and Ruderman 1971; Blandford and Scharlemann 1976; Herold 1979), which for linearly polarized photons may be written as

$$\sigma(1) = \sigma_T \left\{ 1 - \mu_R^2 + \frac{\mu_R^2}{2} \left[ \frac{\omega_R^2}{(\omega_R + \omega_B)^2} + \frac{\omega_R^2}{(\omega_R - \omega_B)^2 + \Gamma^2} \right] \right\},$$

$$\sigma(2) = \frac{\sigma_T}{2} \left[ \frac{\omega_R^2}{(\omega_R + \omega_B)^2} + \frac{\omega_R^2}{(\omega_R - \omega_B)^2 + \Gamma^2} \right]. \quad (7)$$

Here the polarization state 1 corresponds to the photon electric vector  $\epsilon$  in the plane formed by the photon momentum  $\mathbf{k}$  and the field  $\mathbf{B}$ , while state 2 is determined by the condition  $\epsilon_1 \times \epsilon_2 = \mathbf{k}/|\mathbf{k}|$ . Also,  $\mu_R$  is the cosine of the incident photon

angle with respect to  $\mathbf{B}$ ,  $\sigma_T$  denotes the Thomson cross section, and  $\omega_B = eB/mc$  is the cyclotron resonance energy. We have included the Lorentz width  $\Gamma$  in the denominator of the resonant terms, where

$$\Gamma = \frac{4}{3} \alpha m \left( \frac{B}{B_{cr}} \right)^2 \quad (8)$$

is the cyclotron radiation rate (inverse lifetime) of the first excited Landau state (Xia *et al.* 1985). We have not in this work incorporated the fully relativistic form of the magnetic Compton cross section (Herold 1979; Daugherty and Harding 1986), mainly because of the greatly increased computational time and/or table storage costs required. The fully relativistic expressions would involve multiple resonance peaks (associated with intermediate states at higher Landau levels), and in addition should include scattering to "final" states at higher Landau levels. (Electrons scattered to such states would very rapidly emit cyclotron photons as they returned to the ground state, and these photons would make some contribution to the final Comptonized gamma-ray spectrum.) However, the Thomson limit should be a good approximation for the ranges of electron energies, field strengths, and temperatures considered in § III below.

The calculation assumes a dipole field configuration near the pole at the surface of a neutron star of radius  $r_0 = 10^6$  cm, where the field strength dependence with height  $z$  above the star is  $B = B_0[r_0/(r_0 + z)]^3$ . The resonant behavior of the magnetic Thomson cross section (whose unpolarized form is illustrated in Fig. 2) implies that, for a given magnetic field strength, the electron scattering mean free paths in the radiation field are strongly dependent on incident electron energy. In addition, the spatial dependence of the magnetic field above the stellar surface is important. Both of these features are apparent in Figure 3, which shows the mean free paths

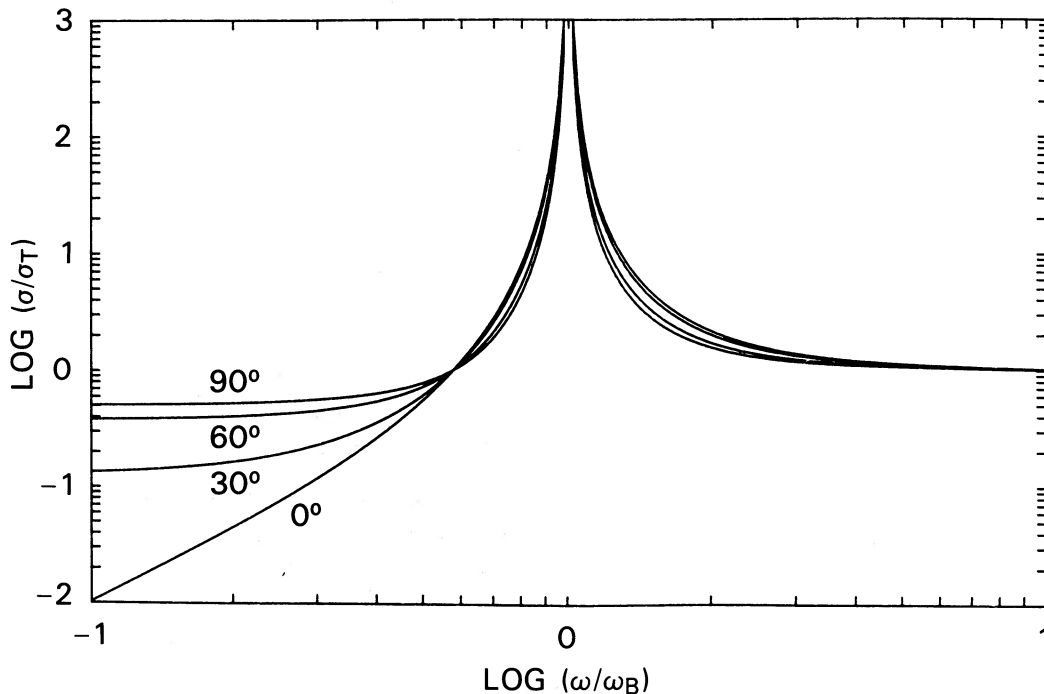


FIG. 2.—Magnetic (resonant) cross section in the Thomson limit (in units of  $\sigma_T$ ) in the rest frame of the incident electron, as a function of incident photon energy  $\omega$  (in units of the cyclotron energy). Cross sections shown at various incident angles are all for unpolarized scattering.



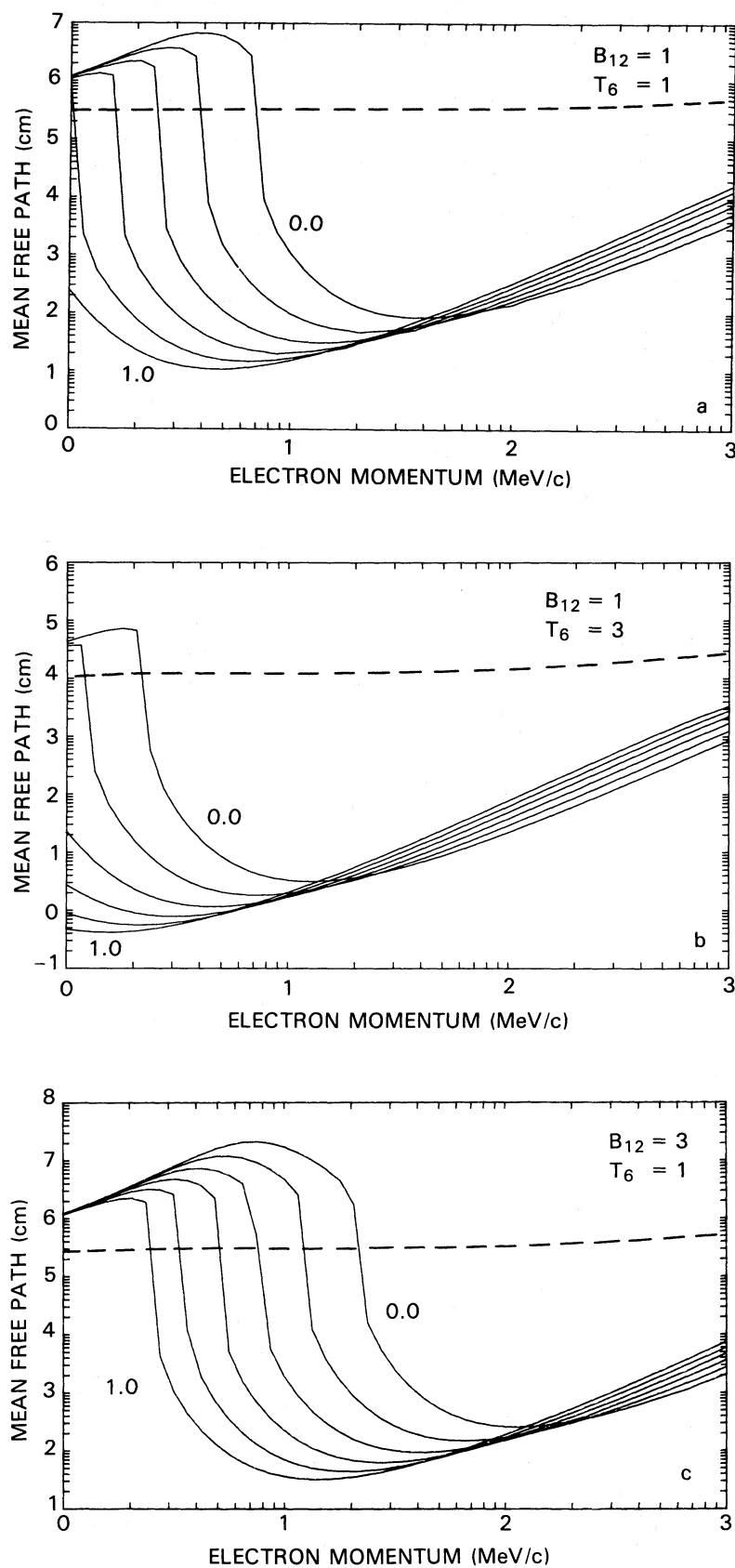


FIG. 3.—Electron mean free paths as a function of energy  $E$ , for (a)  $B_{12} = 1$ ,  $T_6 = 1$ ; (b)  $B_{12} = 1$ ,  $T_6 = 3$ ; (c)  $B_{12} = 3$ ,  $T_6 = 1$ . Curves are plotted for heights ranging from 0 to  $r_0$  above the surface, in steps  $\Delta z = 0.2r_0$  (corresponding to assumed  $z$ -dependence for  $B$ ). Dashed lines indicate nonmagnetic mean free paths at corresponding values of  $T$ .

obtained from adaptive numerical integration of equation (1) with the polarization-averaged cross section of equation (7), for various values of ambient field strength  $B_{12} = B_0/10^{12}$  G and radiation field temperature  $T_6$ . Note that the low-energy portions of these graphs correspond to all RF photon energies lying well below the cyclotron resonance, where the cross section sharply decreases (since in the RF most photons have incident polar angles near  $180^\circ$ ). The slow rise in  $\lambda$  toward increasing energies is due to the apparent decrease of the cyclotron resonance energy (as seen in the RF), and its migration into the low-energy tail of the thermal photon distribution. Since direct evaluation of the mean free paths at each step in an electron trajectory would be prohibitively time-consuming, we have used interpolation of two-dimensional tables of mean free paths versus energy and height.

The sampling of the incident photon energies and polar angles is considerably more difficult than in the field-free case, as may be seen from Figure 4. Here the two-dimensional scattering rate function (the integrand of eq. [1]) may contain a resonant cyclotron "ridge" whenever the thermal photon peak in the RF is near the cyclotron energy,

$$kT[\gamma(1 - v\mu)] \simeq \omega_B. \quad (9)$$

The method we have used to sample this distribution breaks down into two cases. If the incident electron energy is low enough so that the resonant ridge is not present (i.e., if the transformed resonance remains above an effective high-energy cutoff for the thermal spectrum) as in Figure 4a, we use a direct Von Neumann rejection method, as in the nonmagnetic case, to sample the energy and polar angle simultaneously. If the ridge is present, however, we assume that the incident photon will be taken from some point along the ridge, and numerically perform a line integral along the ridge to obtain the (cumulative) probability function. This approach assumes that the width of the ridge (determined by the Lorentz width of the resonance) is nearly constant.

The transformation to the RF of the incident electron is made as in version 1. In this frame, the sampling of the scattered photon polar angle is based on the differential form of the resonant cross section (7), which after summing over polarizations and integrating over azimuths may be written as

$$\frac{d\sigma}{d\mu'_R} = \frac{3\sigma_T}{8} \times \left[ (1 - \mu_R^2)(1 - \mu'^2_R) + \frac{\omega_R^2(\omega_R^2 + \omega_B^2)}{2(\omega_R^2 - \omega_B^2)^2} (1 + \mu_R^2)(1 + \mu'^2_R) \right] \quad (10)$$

As in the field-free case, the selection of the polar angle determines the scattered energy, but in this case the appropriate kinematical relation is given by the (relativistic) expression (Herold 1979)

$$\omega'_R = \{m + \omega_R(1 - \mu_R\mu'_R) - [m^2 + 2m\omega_R\mu_R(\mu'_R - \mu_R) + \omega_R^2(\mu'_R - \mu_R)^2]^{1/2}\} \times (1 - \mu'^2_R)^{-1/2}. \quad (11)$$

Finally, the transformation back to the LF is carried out and the counting tables are updated as in version 1.

### III. SCATTERED PHOTON SPECTRA

#### a) Nonmagnetic Scattering

In the field-free case, we have studied the scattering of both monoenergetic and power-law electron beams in thermal radi-

ation at temperatures characteristic of neutron star polar caps. We find that the electron spectral evolution and the scattered photon spectra are very sensitive to the radiation temperature, as expected from the strong dependence on temperature of mean free path and energy-loss rate (cf. § III). Figure 5 shows the scattered photon spectra at different distances (in stellar radii) from the injection point for the case of monoenergetic injected electrons of energy 100 MeV. The number of injected electrons in this and all other cases is 5000. Figures 6 and 7 show the corresponding results for the case of electrons injected with a power-law energy distribution  $N(E) \propto E^{-p}$  with spectral index  $p = 2$  between energies 1 and  $10^3$  MeV. Figure 8 shows the final ( $z = 1.0r_0$ ) angular distributions of the electrons and scattered photons for the case  $T_6 = 3$ . As expected, the electrons and photons are more spread in angle at lower energies than at higher energies. As the electron beam spreads in angle and loses energy, the transfer of energy to photons through scattering becomes less effective. Photon spectra at successive distances from the beam injection point therefore converge to a "final" photon spectrum. This convergence occurs most rapidly at the highest photon energies, because the highest energy electrons which produce these scattered photons have the largest energy-loss rates. The scattered photon spectra converge faster (in a smaller distance) at the higher temperature, but in both cases the final spectrum forms within a stellar radius.

The final photon spectrum for the power-law electron injection and the lowest incident photon temperature,  $T = 10^6$  K, is a power law of index  $\alpha = 3/2$ , in agreement with the well-known formula  $\alpha = (p + 1)/2$ , where  $p$  is the electron spectral index, derived in the Thomson limit (Blumenthal and Gould 1970). This behavior is expected in the low-temperature case, since the electrons do not lose energy fast enough to cause a change in their spectrum, and since the photon energies are well below  $mc^2$  in the electron rest frame ( $\gamma kT/mc^2 \ll 1$ ), electron recoil is negligible. However, as the incident photon temperature increases to  $3 \times 10^6$  K, the electrons lose energy more rapidly, their spectrum steepens, and the final photon spectrum has an index of 2, equal to the electron spectral index.

#### b) Magnetic Resonant Scattering

We have also calculated the photon spectra resulting from scattering of thermal photons by relativistic electrons in a strong dipole magnetic field of surface strength  $B_0$ . For comparison with the nonmagnetic case, we have chosen the same parameters (monoenergetic injection at 100 MeV or power-law index  $p = 2$ ) for the injected electrons and the same temperatures for the incident photons. As was illustrated by Figures 3 and 4, photons in the peak of a thermal spectrum at  $T \sim 10^6$  K will lie in the fundamental cyclotron resonance of the scattering cross section in the rest frame of some of the relativistic electrons. The mean free paths of electrons with Lorentz factors which shift photons at the thermal peak into the resonance are therefore much smaller than in the nonmagnetic case.

Scattered photon spectra at successive heights above the neutron star surface are shown in Figure 9 for the case of monoenergetic injection and in Figures 10–12 for power-law injection. Because of the much smaller mean free paths in the magnetic field, the electrons suffer much larger energy losses than in the nonmagnetic case. At each height, electrons injected above the energy where their mean free path decreases sharply (cf. Fig. 3) have lost energy in scatterings and are piled up at that energy. This cutoff energy decreases with height as

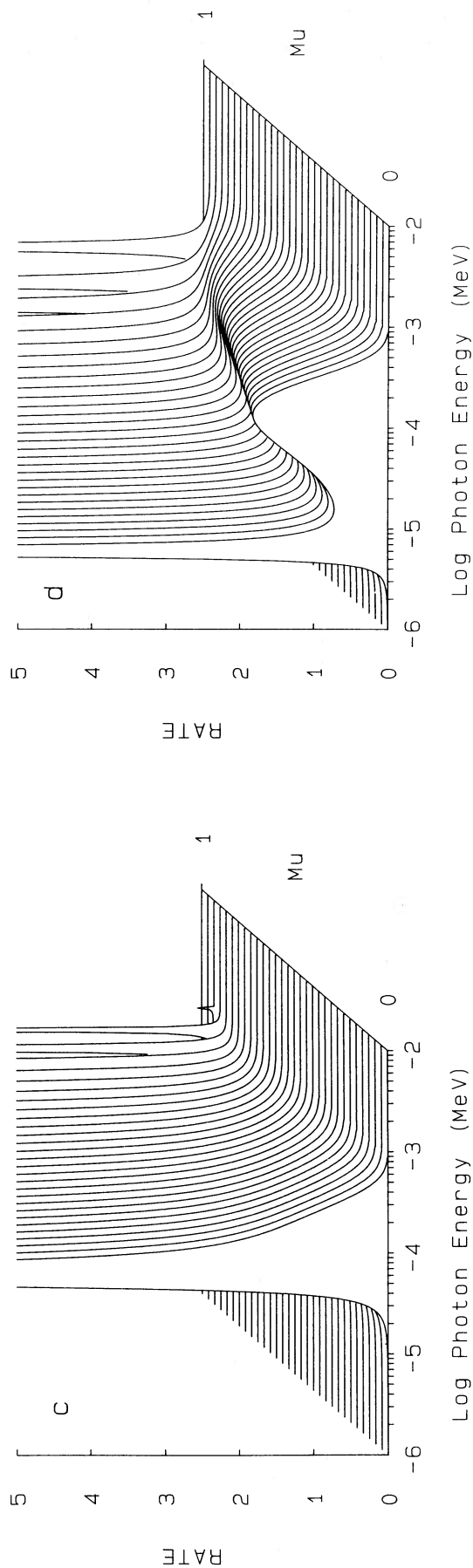
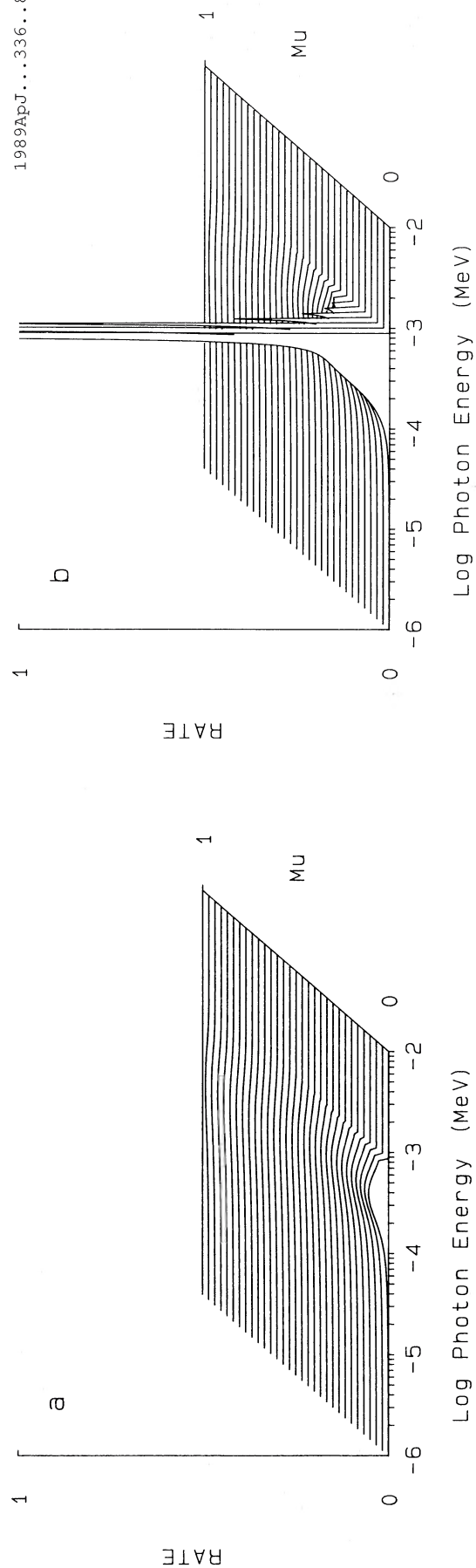


FIG. 4.—Magnetic differential scattering rate function  $R(\omega, \mu)$ , for  $B_{12} = 1$  and  $T_e = 1$ . Plots correspond to the following incident electron energies: (a)  $E = 5$  MeV; (b)  $E = 7$  MeV; (c)  $E = 10^2$  MeV; (d)  $E = 10^3$  MeV.

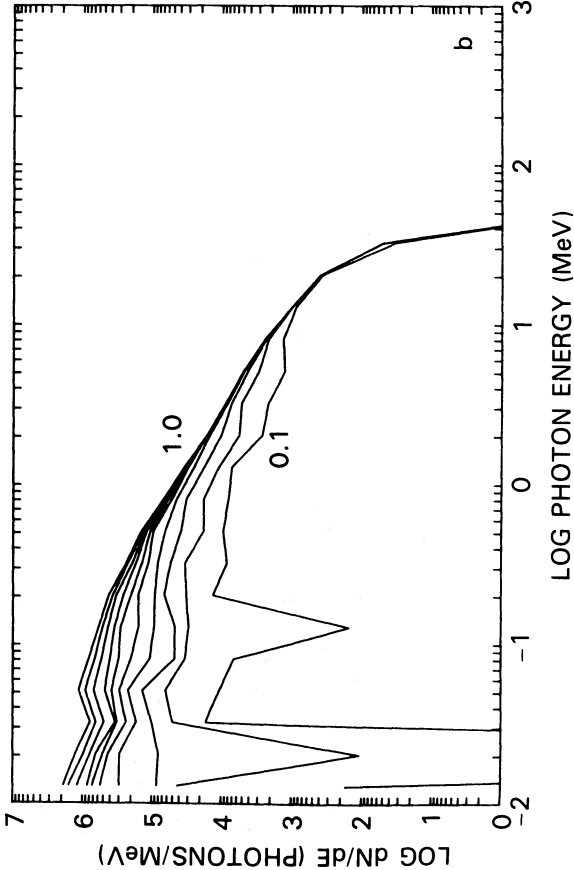
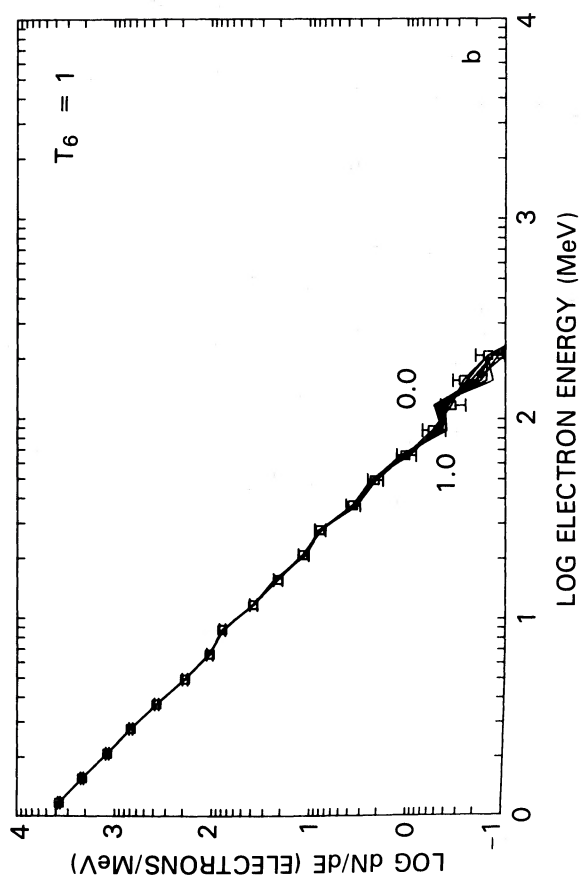
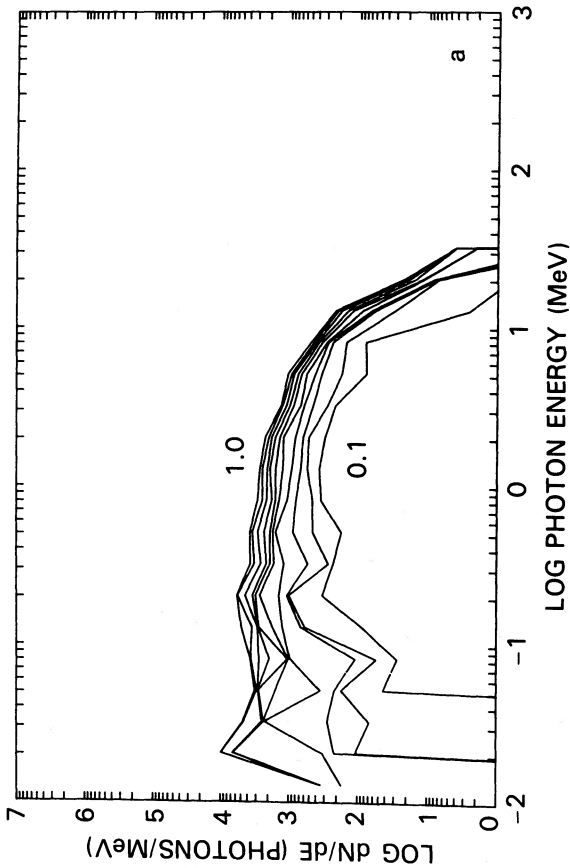
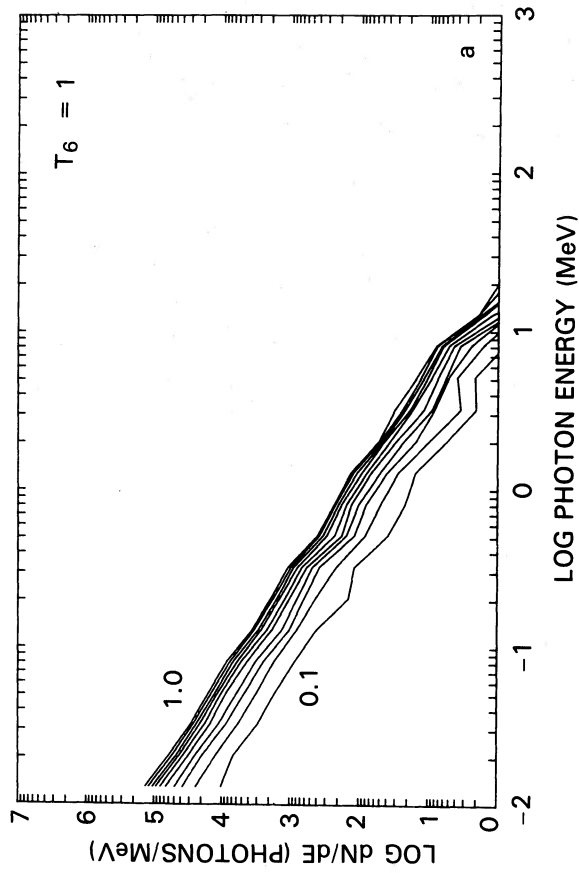


FIG. 5.—Development of Comptonized photon spectrum for nonmagnetic scattering, assuming monoenergetic injected electrons at 100 MeV. Spectra are plotted at height steps  $\Delta z = 0.1r_0$  above the stellar surface, with final spectra at  $r_0$ . (a)  $T_6 = 1$ ; (b)  $T_6 = 3$ .  
 FIG. 6.—Development of (a) photon spectrum and (b) electron spectrum for nonmagnetic scattering, assuming a power-law spectrum for injected electrons (with spectral index 2 over the energy range  $1-10^3$  MeV) and  $T_6 = 1$ . Spectra are plotted at height steps  $\Delta z = 0.1r_0$ , with final spectra at  $r_0$ .



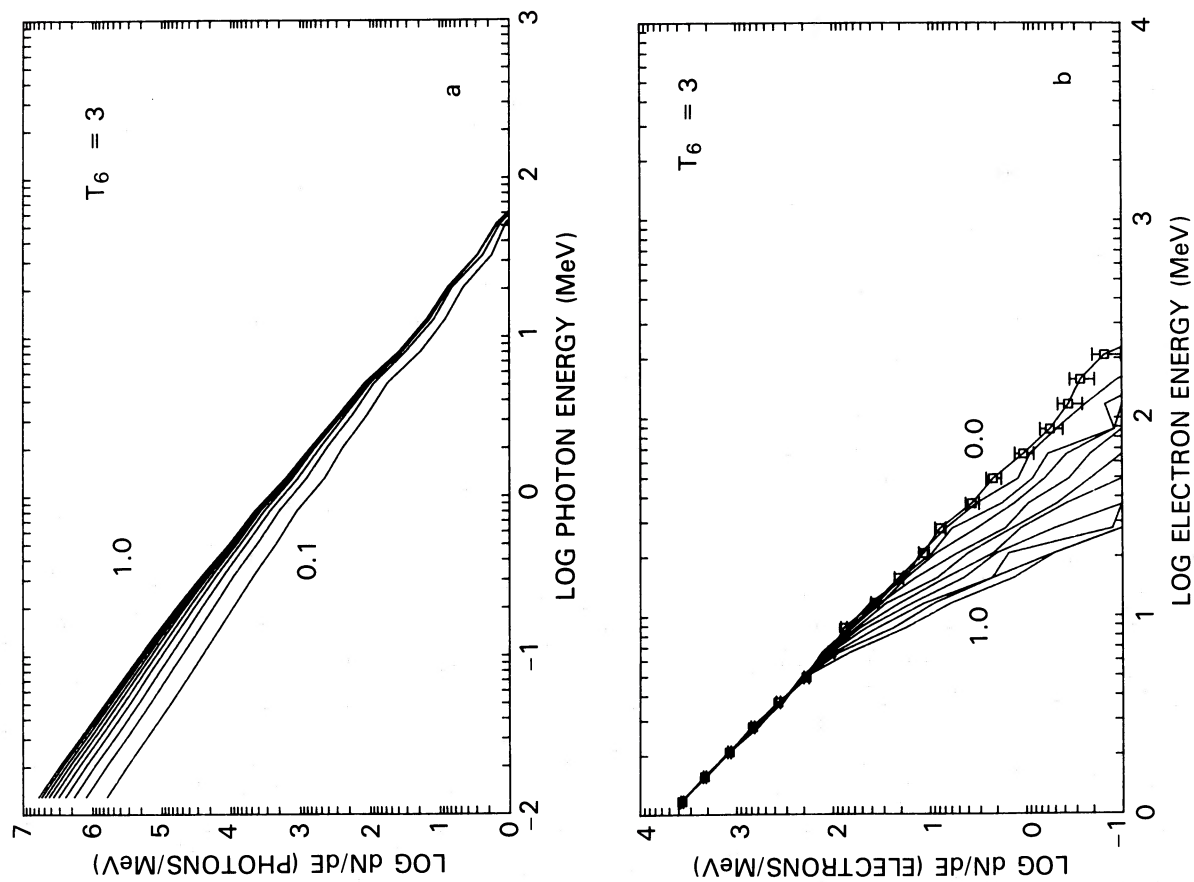


FIG. 7

FIG. 7.—Same as Fig. 6, for  $T_6 = 3$

FIG. 8.—Angular distributions in the laboratory frame of (a) photon and (b) electron beams at a height of  $r_0$ , for  $T_6 = 3$ . The vertical axis shows the particle count in each two-dimensional (energy and polar-angle) bin divided by the respective bin widths. Each curve corresponds to fixed bin energy in MeV, incremented logarithmically at 5 steps per decade for photons and 8 steps per decade for electrons. Polar-angle units on the horizontal axis are  $\Delta\mu = 10^{-2}$  for photons,  $\Delta\mu = 10^{-4}$  for electrons.

FIG. 8

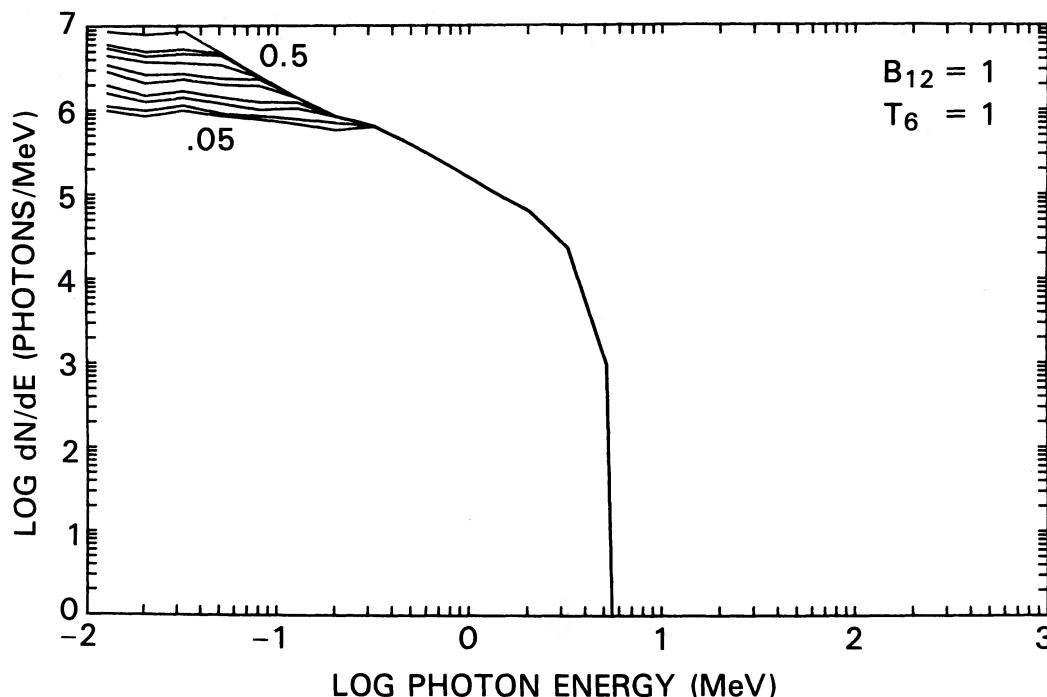


FIG. 9.—Development of Comptonized photon spectrum for magnetic scattering, assuming monoenergetic injected electrons at 100 MeV, for  $B_{12} = 1$ ,  $T_6 = 1$ . Spectra plotted up to  $0.5r_0$  with  $\Delta z = 0.05r_0$ .

the magnetic field strength decreases. Therefore, additional scattered photons appear at low energies as the electrons move away from the surface. With the decreased mean free paths due to resonant scattering, electrons suffer severe energy losses even in the case where  $T = 10^6$  K. The electron energy losses for this same temperature in the nonmagnetic case were negligible. The final photon spectra resulting from resonant scattering therefore in all cases have a power-law index equal to that of the electrons, because of the electron energy losses.

The distance over which the electron beam loses its energy depends sensitively on incident photon temperature and magnetic field strength. For the cases we have considered, the electron beam energy loss rate,  $dE/dz$ , increases with higher  $T$  and lower surface  $B$ , resulting in formation of the final scattered photon spectrum closer to the neutron star surface. A higher temperature increases the photon density and also increases the number of low-energy electrons which can resonant scatter with photons in the blackbody peak (cf. Fig. 3). As the magnetic field increases, the resonance broadens (cf. eq. [18]) but moves to higher energy, increasing the electron energy required to resonant scatter at a given height. Above some field strength (for a given temperature) none of the electrons will resonant scatter near the neutron star surface, where photon densities are high, and  $dE/dz$  will drop dramatically. In general, the distance over which the energy in the injected electron spectrum is converted into scattered photon energy is smaller than in the nonmagnetic case. In the case  $T_6 = 3$ ,  $B_{12} = 1$  (Fig. 11), nearly all of the injected electron beam energy is converted into photon energy in only a quarter of a stellar radius.

Figure 13 shows the angular distribution of the final scattered photons at different energies. The distributions are hollow cones at low energies with opening angle roughly pro-

portional to  $1/\gamma$  and more centrally peaked at high energies. This behavior results from the dependence of the differential scattering cross section (eq. [10]) on energy and angle. The first term, having the dependence  $(1 - \mu_R'^2)$ , dominates for photon energies  $\omega/\omega_B < (1 - \mu_R'^2)^{1/2}/\gamma$ , while the second term, having the dependence  $(1 + \mu_R'^2)$ , dominates for photons in and above the resonance. (Note that the incident photons have  $\mu_R \simeq -1$ ).

#### IV. DISCUSSION

We have shown that resonant scattering can be an important energy-loss mechanism for relativistic electrons and positrons near a hot neutron star surface. If the surface temperature is  $T_6 \sim 6.7B_{12}/\gamma$ , then photons in the blackbody peak will undergo resonant scattering with electrons of energy  $\gamma mc^2$ . This condition may be satisfied in younger pulsars such as the Crab and Vela whose surface temperatures may still be in the  $10^6$  K range. In addition, higher electron energy-loss rates in the presence of a strong magnetic field make Compton scattering a more important source of photons which could contribute significantly to the X-ray and gamma-ray spectra of young pulsars. Unlike the field-free case, surface temperatures of only around  $10^6$  K are required for efficient conversion of energy from relativistic electrons to high-energy photons, and this energy conversion can occur over distances much smaller than a stellar radius. Our results generally confirm the estimates of Blandford and Scharlemann (1976), who found that resonant scattering of thermal radiation near the surface is probably not important for the average pulsar but could be important for younger pulsars such as the Crab.

We found that the spectral index of the scattered photon spectra in the case of resonant scattering will be the same as the injected electron spectral index. The observed photon spectral

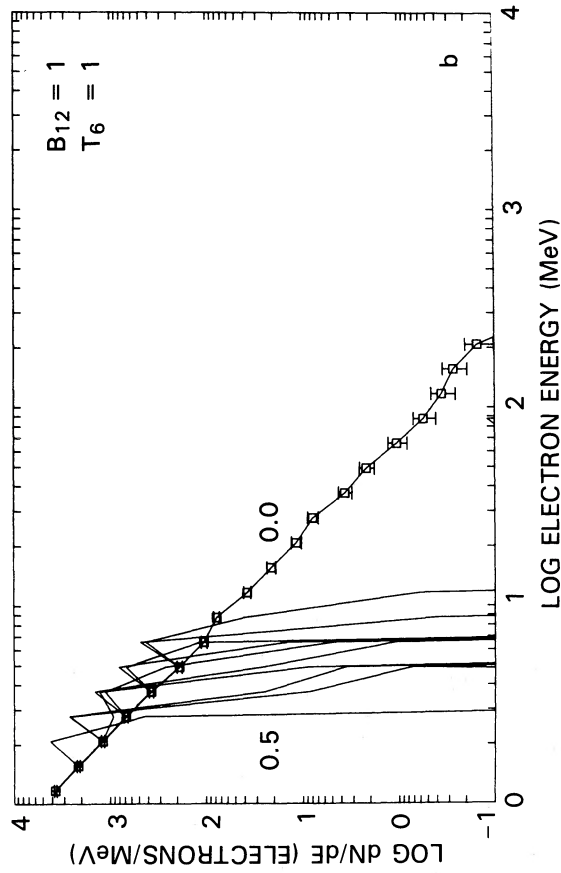
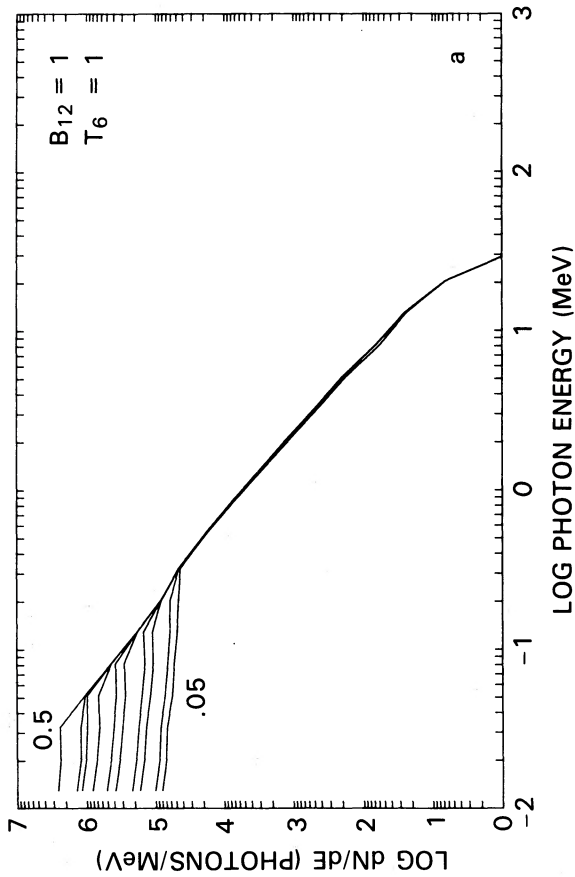


FIG. 10

FIG. 10.—Development of (a) photon spectrum and (b) electron spectrum for magnetic scattering, assuming power-law spectra for injected electrons (with spectral index 2 over the energy range  $1-10^3$  MeV), for  $B_{12} = 1$ ,  $T_6 = 1$ . Spectra plotted up to  $0.5r_0$ , with  $\Delta z = 0.05r_0$ .

FIG. 11.—Same as Fig. 10, for  $B_{12} = 1$ ,  $T_6 = 3$ , and  $\Delta z = 0.025r_0$  (final spectra at  $0.25r_0$ )

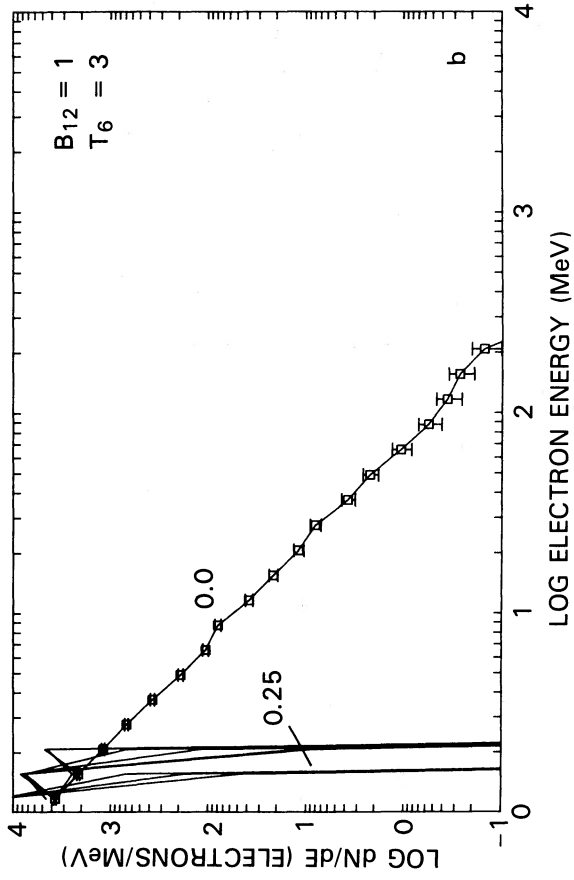
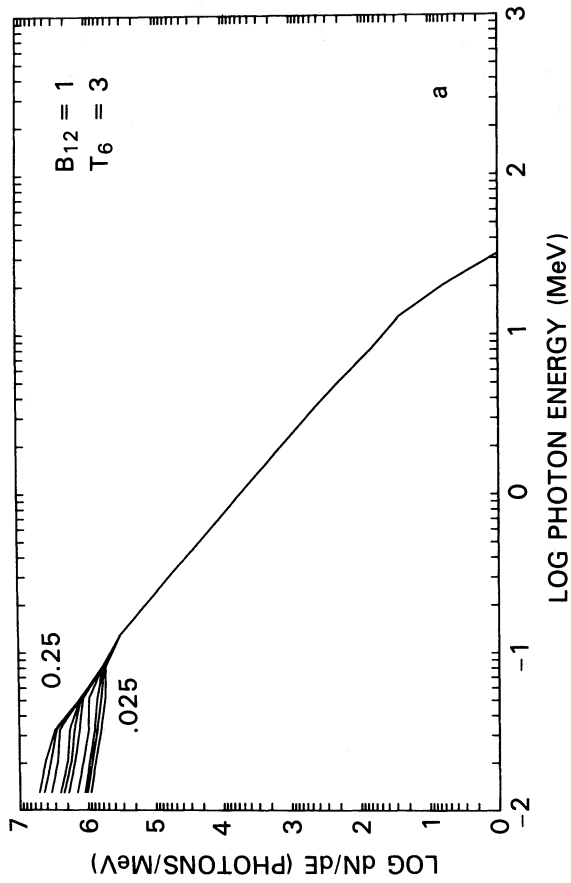


FIG. 11

FIG. 11.—Same as Fig. 10, for  $B_{12} = 1$ ,  $T_6 = 3$ , and  $\Delta z = 0.025r_0$  (final spectra at  $0.25r_0$ )

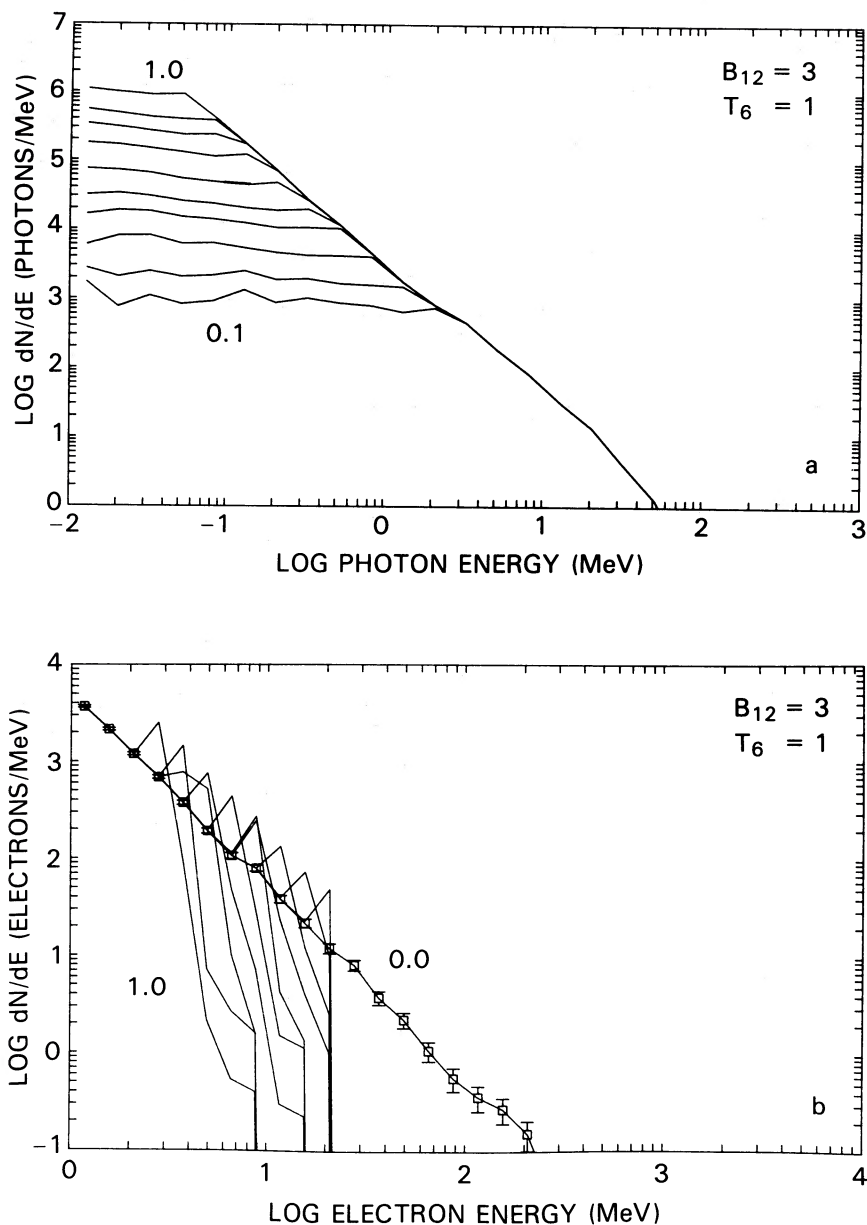


FIG. 12.—Same as Fig. 10, for  $B_{12} = 1$ ,  $T_6 = 3$ , and  $\Delta z = 0.1r_0$  (final spectra at  $r_0$ )

index of the Crab pulsar in the 10 keV to 1 MeV range is  $1.74 \pm 0.02$  (Knight 1982), requiring an injected electron (or pair) spectrum with the same index to explain this emission in terms of resonant Compton scattering near the surface. Pair spectra with indices between 1.5 and 2 have been produced in simulations of polar cap cascades (Daugherty and Harding 1982), so a Compton scattering contribution to the Crab spectrum might be reasonable and requires about  $10^{35} \text{ ergs s}^{-1}$  in pairs. However, if the temperature of the Crab is near the measured upper limit of  $3 \times 10^6 \text{ K}$ , then surface emission models might have difficulty avoiding attenuation of the observed GeV gamma rays by pair production with the thermal X-ray photons.

On the other hand, the more efficient the energy loss of relativistic electrons through scattering, the more possibly dis-

ruptive it is to other processes that are expected to take place in polar cap pulsar models. Scattering would probably not interfere with synchrotron radiation from secondary pairs from an electromagnetic cascade near the surface (Daugherty and Harding 1982) because of the extremely high radiation rates in strong magnetic fields. However, the radio emission mechanism requires electrons and positrons with  $\gamma \sim 100$  for coherent curvature radiation. If temperatures are large enough to satisfy conditions for resonant scattering of the pairs, then the creation of the radio-emitting pairs could not take place too close to the stellar surface or the energy of the pairs would be converted into high-energy photons rather than into radio photons. Resonant scattering could also be an important energy-loss mechanism for the primary electrons, competing both with electrostatic acceleration and curvature radiation



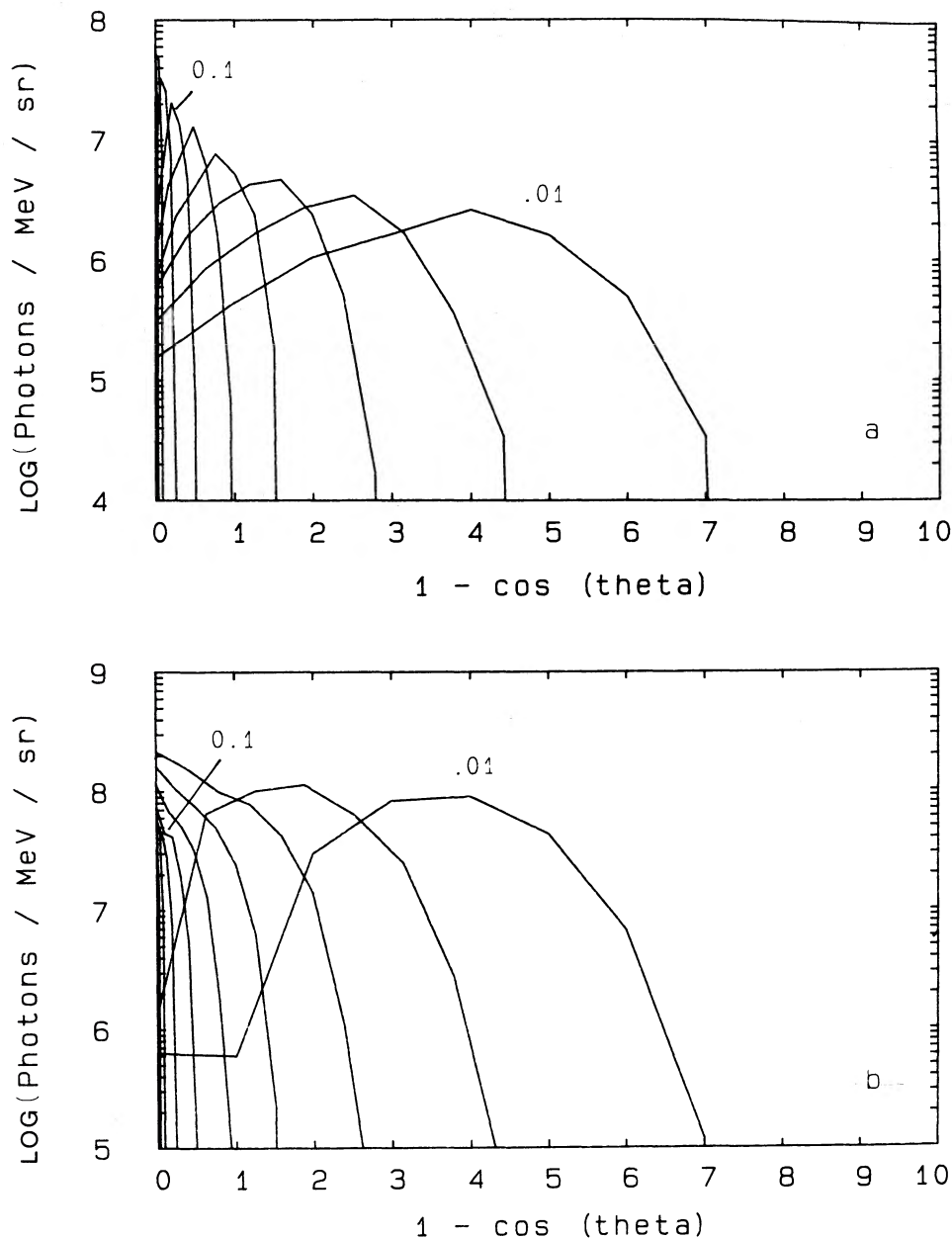


FIG. 13.—Angular distributions of photons in the laboratory frame at heights (a)  $0.05r_0$  and (b)  $0.5r_0$ , for  $B_{12} = 1$ ,  $T_6 = 1$ . Here the vertical axis shows the particle count in each two-dimensional (energy and polar-angle) bin divided by the respective bin widths. Each curve corresponds to fixed bin energy in MeV, incremented logarithmically at 5 steps per decade. Polar-angle units are  $\Delta\mu = 10^{-2}$ .

losses (Xia *et al.* 1985). However, temperatures in excess of  $3 \times 10^6$  K are required in order to place limits on polar cap acceleration models having electric fields in the range  $10^8$ – $10^{10}$  V cm $^{-1}$ .

We would like to thank M. Elitzur, C. D. Dermer, and F. C. Jones for helpful discussions, and M. McMullen for programming assistance. J. K. D. acknowledges partial support from The Research Corporation.

#### REFERENCES

- Arons, J. 1983, *Ap. J.*, **266**, 215.  
 Berestetskii, V. B., Lifshitz, E. M., and Pitaevskii, L. P. 1982, *Quantum Electrodynamics* (New York: Pergamon).  
 Blandford, R. D., and Scharlemann, E. T. 1976, *M.N.R.A.S.*, **174**, 59.  
 Blumenthal, G. R., and Gould, R. J. 1970, *Rev. Mod. Phys.*, **42**, 237.  
 Canuto, V., Lodenguai, J., and Ruderman, M. 1971, *Phys. Rev. D*, **3**, 2303.  
 Cheng, A. F., and Ruderman, M. A. 1977, *Ap. J.*, **216**, 865.  
 Cheng, K. S., Ho, C., and Ruderman, M. A. 1986, *Ap. J.*, **300**, 500.  
 Daugherty, J. K., and Harding, A. K. 1982, *Ap. J.*, **252**, 337.  
 ———. 1986, *Ap. J.*, **309**, 362.  
 Elitzur, M. 1979, *Ap. J.*, **229**, 742.  
 Gold, T. 1968, *Nature*, **218**, 731.  
 Harnden, F. R., Grant, P. D., Seward, F. D., and Kahn, S. M. 1985, *Ap. J.*, **299**, 828.  
 Harnden, F. R., and Seward, F. D. 1984, *Ap. J.*, **283**, 279.  
 Heitler, W. 1954, *The Quantum Theory of Radiation* (New York: Dover).  
 Helfand, D. J., Chanan, G. A., and Novick, R. 1980, *Nature*, **283**, 337.  
 Herold, H. 1979, *Phys. Rev. D*, **19**, 2868.  
 Jones, F. C. 1968, *Phys. Rev.*, **167**, 1159.  
 Knight, F. K. 1982, *Ap. J.*, **260**, 538.

- Morini, M. 1983, *M.N.R.A.S.*, **202**, 495.  
Ochelkov, Yu. P., and Usov, V. V. 1983, *Ap. Space Sci.*, **96**, 55.  
Reynolds, S. P. 1982, *Ap. J.*, **256**, 38.  
Ruderman, M. A., and Sutherland, P. 1975, *Ap. J.*, **196**, 51.  
Schlickeiser, R. 1980, *Ap. J.*, **236**, 945.  
Sturrock, P. A. 1971, *Ap. J.*, **164**, 529.  
Tademaru, E., and Greenstein, G. 1974, *Nature*, **251**, 39.  
Xia, X. Y., Qiao, G. J., Wu, X. J., and Hou, Y. Q. 1985, *Astr. Ap.*, **152**, 93.

J. K. DAUGHERTY: Computer Science Department, University of North Carolina at Asheville, Asheville, NC 28804

A. K. HARDING: Code 665, NASA/Goddard Space Flight Center, Greenbelt, MD 20771